Scientific Research Publishing

Journal of Water Resource and Protection, 2026, 18(2), 132-152
https://www.scirp.org/journal/jwarp
ISSN Online: 1945-3108
ISSN Print: 1945-3094

Contribution of Remote Sensing to Groundwater Prospecting in Fractured Environments: The Case of Pointe-Noire (Southern Republic of Congo)

Jean Bienvenu Dinga[1,2*], Bonaventure Malonga[1,2], Christ Madzo Makouezi Mokomba[1,2]

[1]Faculté des Sciences et Techniques, Université Marien Ngouabi, Brazzaville, The Republic of Congo
[2]Institut National de Recherches en Sciences Exactes et Naturelles (IRSEN), Cité Scientifique (Ex-ORSTOM), Brazzaville, The Republic of Congo
Email: *bvs_dinga@yahoo.fr

How to cite this paper: Dinga, J.B., Malonga, B. and Mokomba, C.M.M. (2026) Contribution of Remote Sensing to Groundwater Prospecting in Fractured Environments: The Case of Pointe-Noire (Southern Republic of Congo). *Journal of Water Resource and Protection*, **18**, 132-152.
https://doi.org/10.4236/jwarp.2026.182008

Received: November 3, 2025
Accepted: February 7, 2026
Published: February 10, 2026

Abstract

This study focuses on the city of Pointe-Noire, in the south-west of the Republic of Congo, where invoicing is more or less developed. Its main objective is to map fractured environments in order to improve groundwater prospecting by combining Landsat 8 OLI & TIRS images with SRTM data. To achieve this objective, we collected a Landsat 8 OLI & TIRS scene dating from February to August 2020 from the USGS database and ten (10) SRTM tiles from the JAXA database. All techniques applied to Landsat 8 OLI and TIRS images (PCA, textural analysis, band ratio, normalised indices, Sobel, Prewitt and Yesou directional gradient filters) using ENVI 5.3 resulted in the enhancement of linear structures contained in the raw images, extracted using GEOMATICA, enabling better mapping of geological hazards in QGIS 3.16. The linear map obtained after automatic extraction is very dense and contains linear features of varying sizes and orientations. After submitting the lineaments obtained from automatic extraction to Pareto's statistical test, followed by their merging with the lineaments obtained from manual extraction, the various linear structures were validated by adapting their orientations to the tectonic context of the area and superimposing them of the existing geological map and topographical map (from Google Earth pro), this led to the creation of the final lineament map of the study area, comprising 750 lineaments. Analysis of the lineament spacing and texture revealed the homogeneity of the geological formations in the study area, a comparison of fracturing densities between the

2015 data (more specifically the 1980 data used) and those from our study shows, on the one hand, the dominance of NW-SE and E-W orientations in the area, thus influencing the surface hydrographic network and groundwater recharge and, on the other hand, allows us to assess the evolution of tectonic activity. The results of this work contribute to a better understanding of fractured environments in the city of Pointe-Noire.

Keywords

Lineaments, Remote Sensing, Fractured Environments, Groundwater Prospecting, Landsat 8, Pointe-Noire

1. Introduction

The Republic of Congo has abundant surface and groundwater resources. However, despite this abundance, some cities in Congo, notably the economic city of "Pointe-Noire", experience water supply difficulties, according to [1]. Less than half of the Congolese population, and only 10% of households in rural areas, have access to drinking water. People are therefore forced to use boreholes to collect water from underground aquifers. Facture networks are the main channels for underground flows. Studying fracture networks, which are the main pathways for underground flows, is fundamental to groundwater exploration. Indeed, most resources are found in fractured aquifers [2]-[4]. Billing can be studied using several different methods such as remote sensing (aerial and satellite photographs, radar imagery) and geophysics. Remote sensing involves multiple techniques or methods of pre-processing and processing that enhance the visual perception of the images acquired for better mapping of image discontinuities. Numerous studies [5] [6] demonstrated how remote sensing can contribute to hydrogeological investigations. The works of [2] [3] highlighted the relationship between remote sensing data and groundwater resources in bedrock. It was shown that satellite images contain geological features that are directly linked to groundwater flow [7]. These various studies have contributed to the recognition of the importance of faults in hydrogeology [8]. The mapping of lineaments using satellite imagery [9]-[11] the hydrogeological characterisation of fractured aquifers [11] [12], hydrogeological and hydrochemical in situ study and hydrodynamic modelling of an aquifer system in a coastal sedimentary basin [13] [14], to understand the behaviour of aquifers and map areas of groundwater accumulation or circulation[9] [15] thanks to space imagery fractured aquifer scan be characterised [2]-[4] and fracture lengths vary in size and range over several orders of magnitude [4] [9] [14] [16]-[18]. The work of [19]-[21] has shown that extracting the network of major fractures from satellite images is very important for groundwater exploration. Directional filters also allow the perception of lineaments that are not well lit by the light source [16] [19]. For this work, a passive remote sensing technique

using: Landsat 8 OLI & TIRS is applied in the city of Pointe-Noire.

2. Presentation of the Study Area

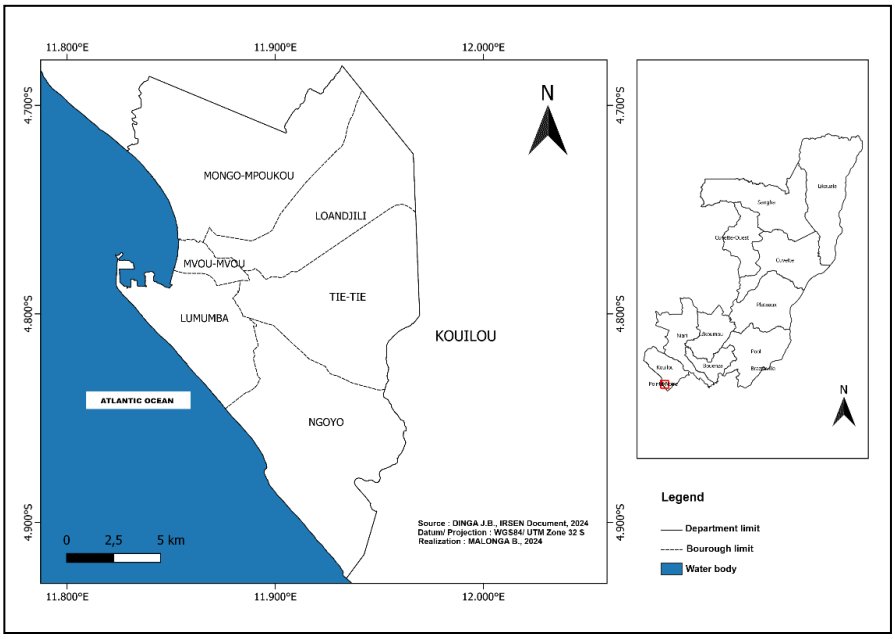

Figure 1. Geographical location of the study area.

The study area is the city of Pointe-Noire, located in the Sud-Ouest of the Republic of Congo between 11˚30 and 12˚ East longitude 4˚30 and 5˚ South latitude (**Figure 1**). It covers an area of approximately 2.134 km^2 and stretches 180km along the coastline, which runs SE-NW. It's bordered to the north by the Red River (near the site of Loango), to the south by the site of Djeno and the Atlantic Ocean, to the east by the large railway station of Ngandji, Ex-patra, and to the west by the Atlantic Ocean. Pointe-Noire is also a department located approximately 510 km from Brazzaville, the political capital. As the country's economic capital, it is home to the largest port in Central Africa. Administratively, it has six (6) boroughs (**Figure 1**). The climate is humid tropical [22] [23] characterised by alternating hot rainy seasons (October-May) and cool dry seasons (June-September) [23] [24]. Average annual rainfall is approximately 1300 mm [22] [23]. The terrain consists three main elements: plateaus, large valleys and a coastal plain. The altitude is generally less than 150 m [22]. The landscape is dominated by a forest-savanna mosaic [22]. The hydrographic network is organised around three types of watercourses [22]: the short rivers that originate on the western edge of the coastal plateau and the Kouilou River. Its average flow is 913 m^3/s at Sounda and 1150 m^3/s at the mouth. The different types of soils found in the study area belong mainly to four classes [24]: poorly developed soils, hydromorphic soils, podzolic soils and ferralitic soils, which are highly desaturated and by far the most common. All soils are derived from the original loose materials which are sands from the cirque series

[24]. The cirque series (or Diosso serie), dating from the Miocene to Pliocene epochs, forms a fluvial to deltaic covering the entire coastal basin and resting unconformably on the Mesozoic substratum [24]. From a structural point of view, there are three (3) fault systems [24], a system of faults oriented NW-SE parallel to the mayombian structures, a system of perpendicular faults NNE-SSW à NNW-SSE that delimit the horst and ridge structures, and a system of faults E-W that controls the Mesozoic series at the Mayombian border. The study area features six (6) geological formations [24] heterogenous sand to orange-yellow sandy loango (cover horizon, rocks sedimentary), and stone line; deposits (colluvional deposits, slope deposits); current coastal zone (coastal deposits, current beach sand); vegetated dune cordon behind the beach (deposits, beach dune behind the beach); the rocky banks (rocky bottoms); and white to grey colluvial quartz sand on slopes or the bottom (dry valleys) (**Figure 2**).

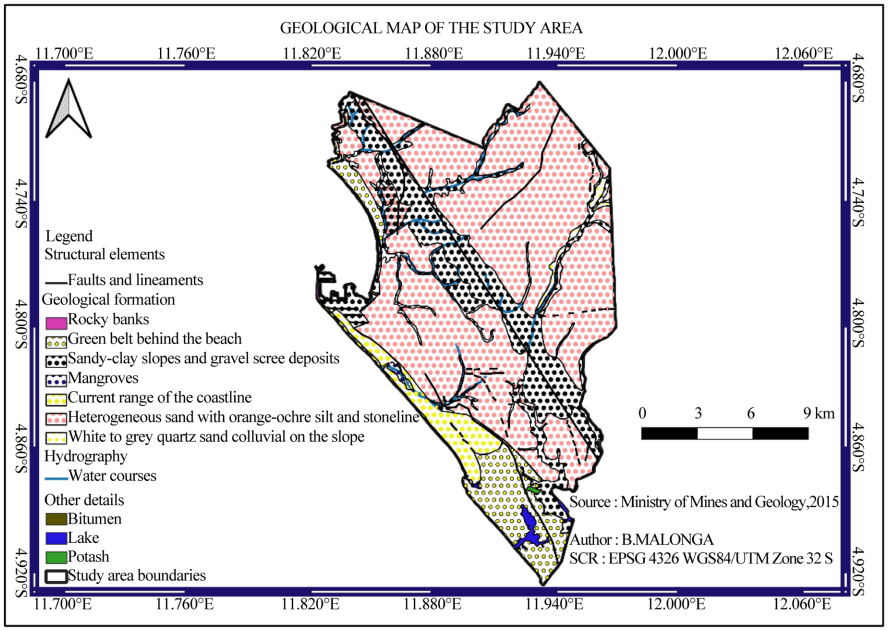

Figure 2. Geological map of the study area (Source: Ministry of Mines and Geology, 2015).

3. Material and Methods

3.1. Material

3.1.1. Data used

✓ ***The images LANDSAT 8 OLI & TIRS***

The multitemporal Landsat 8 OLI (*Operational Land Imager*) & TIRS (*Thermal InfraRed Sensor*) images data used were acquired on 20 February 2020 at 09:22:53 and 22 August 2020 at 21:11:20, respectively, during the Landsat space mission of the Landsat programme, developed by NASA in 1960. This is the first space programme for earth observation for civilian [25] purposes, and these data have been archived in the USGS database [26]. **Table 1** shows the Characteristics of the OLI & TIRS sensors on the Landsat 8.

✓ ***The SRTM images***

SRTM images (Shuttle Radar Topography Mission) are images from topographic satellites [27]. The images used are DSM images from the JAXA website [28].

✓ ***The geological map***

As part of our work, we used the geological map of Pointe-Noire (**Figure 2**), produced by the Ministry of Mines and Geology and BRGM Pointe-Noire sheets [24].

✓ ***The topographical map***

A high-resolution topographical map of Pointe-Noire by Google Earth Pro.

Table 1. Characteristics of the OLI & TIRS sensors on the Landsat 8 satellite.

Number of bands	Spectrale band names	Wavelenghts (µm)	Spatial Resolution (m)
1	Aerosols	0.433 - 0.453	30
2	Blue (B)	0.450 - 0.515	30
3	Green (G)	0.525 - 0.600	30
4	Red (R)	0.630 - 0.680	30
5	Near Infrared (NIR)	0.845 - 0.885	30
6	Mid-Infrared 1 (SWIR-1)	1.560 - 1.660	30
7	Mid-Infrared 2 (SWIR-2)	2.100 - 2.300	30
8	Panchromatic	0.500 - 0.680	15
9	Cirrus	1.360 - 1.390	30
10	Thermal Infrared Sensor 1 (TIRS-1)	10.60 - 11.20	100
11	Thermal Infrared Sensor 2 (TIRS-2)	11.50 - 12.50	100

3.1.2. Software Used

Three software were used for this work ENVI 5.3 [29] for pre-processing and processing GEOMATICA 19.0 for automatic extraction and QGIS 3.16 for map creation as well as EXCEL office software for statistical analysis of lineaments.

3.2. Methods

The appropriate methodological approach is summarised in the figure (**Figure 3**).

During the pre-processing phase (radiometric and atmospheric corrections), two bands were discarded (8 and 9) in order to correct the image. The image corrected by principal component analysis will be filtered by directional filtering on the PCA_{234}; PCA_{567}; PCA_{6710}; PCA_{671011}; the raw bands B4; B6; B7, the bands ratios B6/B5; B5/B7, on the colour compositions, three types of directional filtering were applied: Sobel filter, and Prewitt and Yesou gradient filters using ENVI 5.3 software. In PCA, this technique is used to identify the axes of greatest variance in the radiometric space of an image. The aim is to map the main features of the fracture in our study area, to this end, selective PCA was performed on the visible (2,3,4),

mid-infrared (5, 6, 7) and thermal infrared (10, 11).

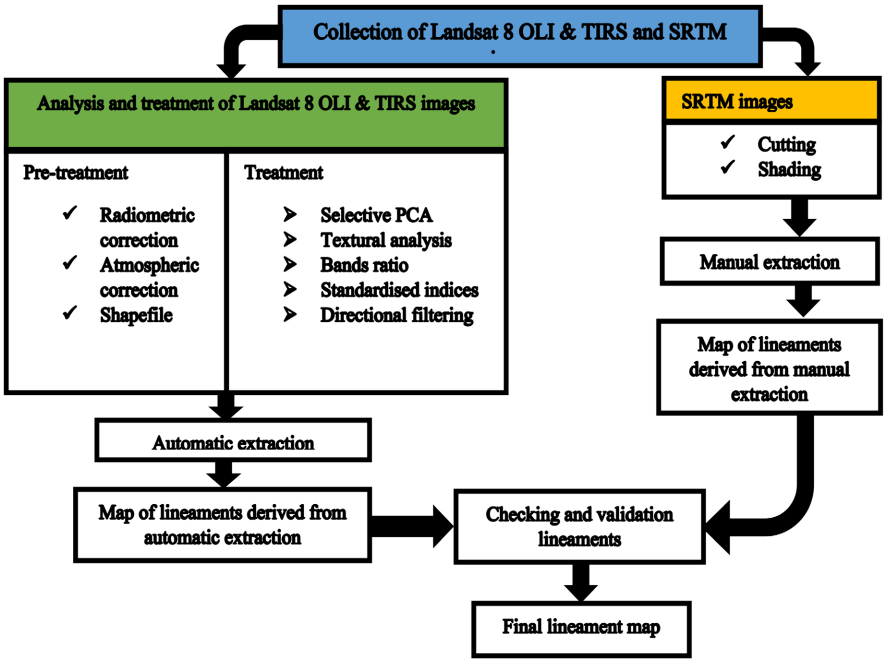

Figure 3. Overall flowchart of the methodology adopted (pre-processing and processing).

The Sobel filter was applied using the following directions: N-S (0˚); E-W (90˚); NE-SW (45˚) and NW-SE (135˚): only two directions were presented for this work in relation to the tectonic of the study area: E-W and NW-SE. After processing the Landsat 8 OLI images, we proceeded with two types of lineament extraction on QGIS using SRTM images under directional shading, 0˚; 45˚; 90˚; 135˚, and automatic extraction on GEOMATICA. After obtaining the lineaments, a map of the total fusion of the lineaments (manual and automatic) was established. The validation of these lineaments and the creation of the final lineament map were carried out by evaluating their orientation and adapting them to the tectonic context of the study area. A Pareto statistical test was performed on the lineaments in order to select them and assess their reliability. It is based on the 80/20 or 85/15 rule, which suggests that in many cases approximately 80% of the effects come from 20% of the causes [30]. This test is performed in Excel using diagrams. The Pareto curve is less frequent or less significant than those above it.

We note that satellite images used *i.e.* a single scene from Landsat 8 OLI & TIRS, have certain characteristics, namely 11 bands: three visible bands, three mid-infrared bands and thermal infrared bands, two of which (8 and 9) have been removed in order to achieve perfect correction of the image (shapefile). Each directional filter (Sobel) was used with its corresponding orientation, with the exception of the Prewitt and Yesou gradient filters. For automatic extraction using the methodology, six (6) parameters were applied to the filtered images using the LINE module of the GEOMATICA PCI software.

Table 2 shows the different directional filters used.

Table 2. Different directional filters used.

Directional Sobel Filter N-S							Directional Sobel Filter E-W						
1	1	1	2	1	1	1	−1	−1	−1	0	1	1	1
1	1	2	3	2	2	1	−1	−1	−2	0	2	1	1
1	2	3	4	3	3	1	−1	−2	−3	0	3	2	1
0	0	0	0	0	0	0	−2	−3	−4	0	4	3	2
−1	−2	−3	−4	−3	−3	−1	−1	−2	−3	0	3	2	1
−1	−1	−2	−3	−2	−2	−1	−1	−1	−2	0	2	1	1
−1	−1	−1	−2	−1	−1	−1	−1	−1	−1	0	1	1	1
Directional Sobel Filter NE-SW							Directional Sobel Filter NW-SE						
0	1	1	1	1	1	2	2	1	1	1	1	1	0
−1	0	2	2	2	3	1	1	3	2	2	2	0	−1
−1	−2	0	3	4	2	1	1	2	4	3	0	−2	−1
−1	−2	−3	0	3	2	1	1	2	3	0	−3	−2	−1
−1	−2	−4	−3	0	2	1	1	2	0	−3	−4	−2	−1
−1	−3	−2	−2	−2	0	1	1	0	−2	−2	−2	−3	−1
−2	−1	−1	−1	−1	−1	0	0	−1	−1	−1	−1	−1	−2
Prewitt Filter							Yesou Filter & al (1993)						
1	1	1	1	1	1	1	1	1	1	1	1	1	0
1	1	1	1	1	1	1	1	1	1	1	1	1	1
1	1	1	1	1	1	1	1	1	1	1	1	1	1
−1	−2	−3	−7	1	1	1	0	0	0	0	0	0	−1
−1	−2	−3	−3	1	1	1	−1	−1	−1	−1	−1	−1	−1
−1	−2	−2	−2	1	1	1	−1	−1	−1	−1	−1	−1	−1
−1	−1	−1	−1	1	1	1	−1	−1	−1	−1	−1	−1	−1

Table 3. Values used of the parameters of the PCI LINE module.

Name	RADI	GTHR	LTHR	FTHR	ATHR	DTHR
Meaning	Pixel filter radius	Threshold for edge gradient	Threshold for curve length	Threshold for line assembly error	Angular difference threshold	Threshold for the link distance
Number of pixels	50	100	50	50	-	100
Angle (˚)	-	-	-	-	30	-
Length (km)	1.5	3	1.5	1.5	-	3

This produces a summary lineament map, which is then superimposed on the high-resolution topographic map on Google Earth Pro, eliminating other linea-

ments to finally obtain the final lineament map of the study area.

Table 3 shows the values used for the parameters of the PCI line module.

4. Results and Discussion

4.1. Results

4.1.1. Pre-Treatment Results

a) Results of radiometric and atmospheric corrections using the radiometric correction algorith

Figure 4 shows the results of radiometric and atmospheric correction.

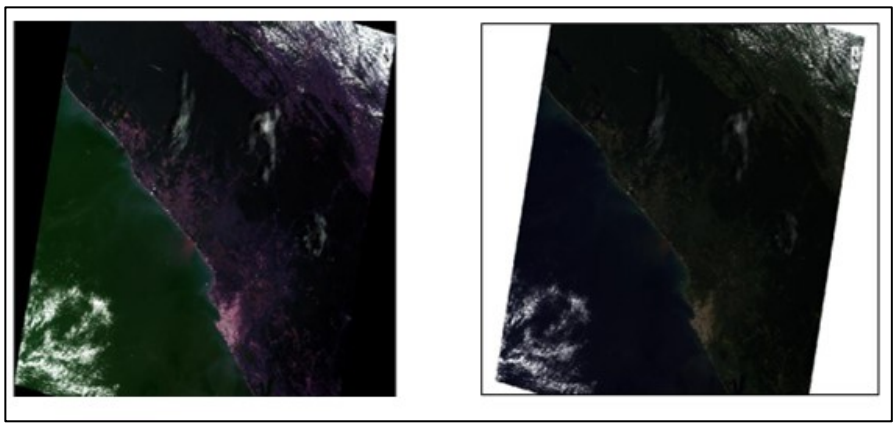

Figure 4. Results of radiometric and atmospheric correction.

4.1.2. Treatment Results

a) Textural analysis results obtained used the co-occurrence measures algorithm

The textural analysis of PCA_{234} and on individual band 4 (Figure 5) shows a significant distinction on vegetated surfaces, the first image has a green appearance with dotted structures, while the second image has a dark blue appearance with linear features.

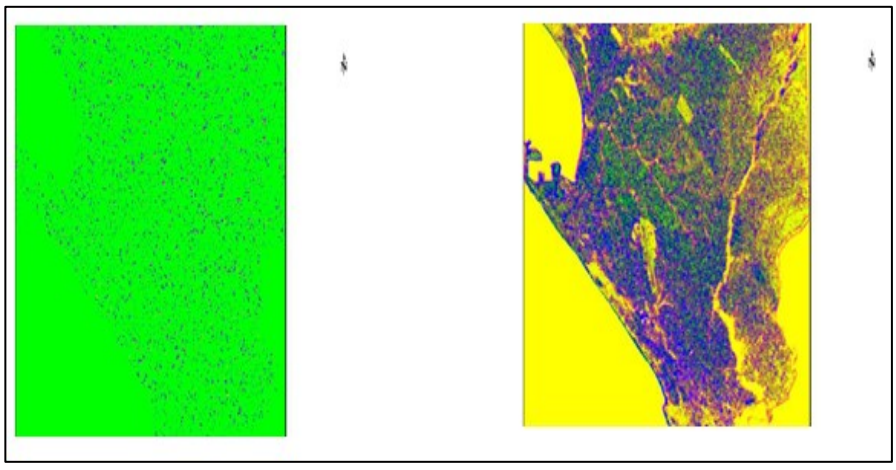

Figure 5. Results of the textural analysis applied to PCA234 and B4.

b) Results of principal component analyses applied to the bands 2, 3, 4, 5, 6, 7, 10 et 11 used the PCA Rotation

The PCA selective of the different bands (Figure 6) already point us towards directional filtering, despite the characteristics present in these images.

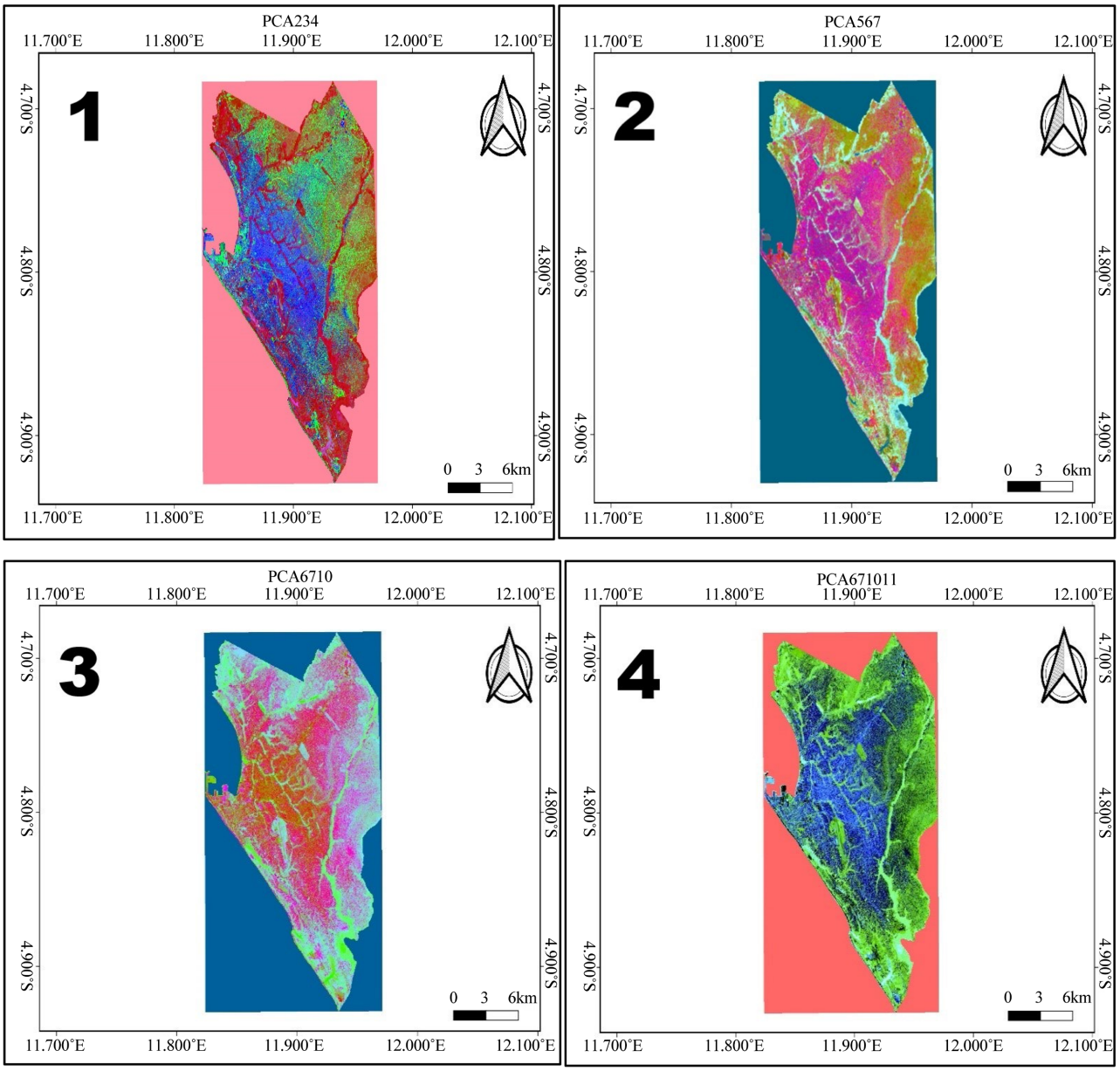

Figure 6. Results of principal component analysis 1. PCA_{234}; 2. PCA_{567}; 3. PCA_{6710} and 4. PCA_{671011}.

c) Results of colour compositions obtained via the RGB Band Change algorithm

The colour compositions of the OLI visible and TIRS thermal bands (Figure 7) shows variations on the surface where linear structures or geological features can already be observed.

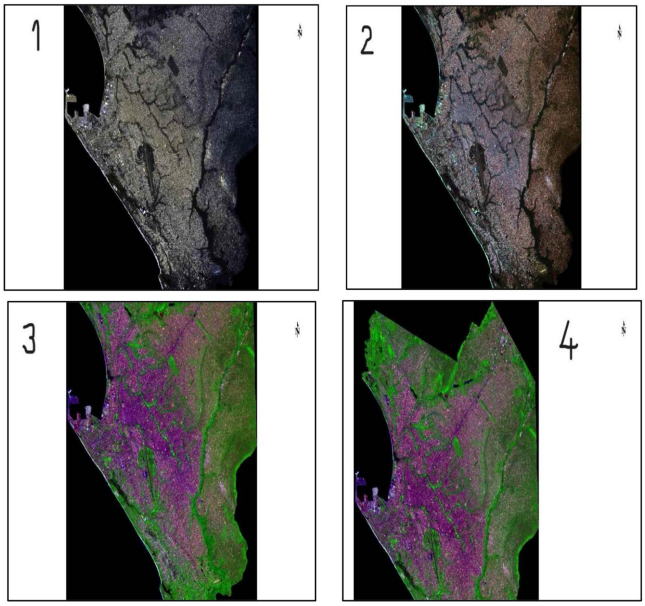

Figure 7. Results of colour compositions: 1. True colour 2, 3, 4; and false colours: 2. 7, 3, 1; 3. 7, 5, 4 and 4. 7, 5, 2.

d) Results obtained by band ratios

These band ratios (Figure 8) show the visibility of fractures with a dark grey and light appearance on the surface of each scene or image.

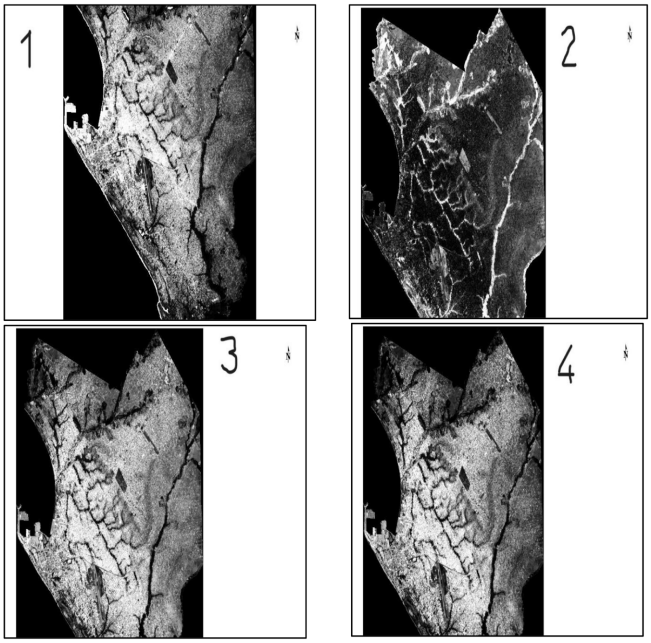

Figure 8. Results of the ratio of bands, 1. B4/B5; 2. B5/B6; 3. B6/B5 and 4. B7/B5.

e) Result of the Sobel filter with NW-SE direction and 135˚ angle by applying Convolution of morphology on ENVI

The Sobel filter in the images above (Figure 9) shows a significant characteristic

of the linear structures that can be extracted by applying the Convolution of morphology algorithm in ENVI 5.3.

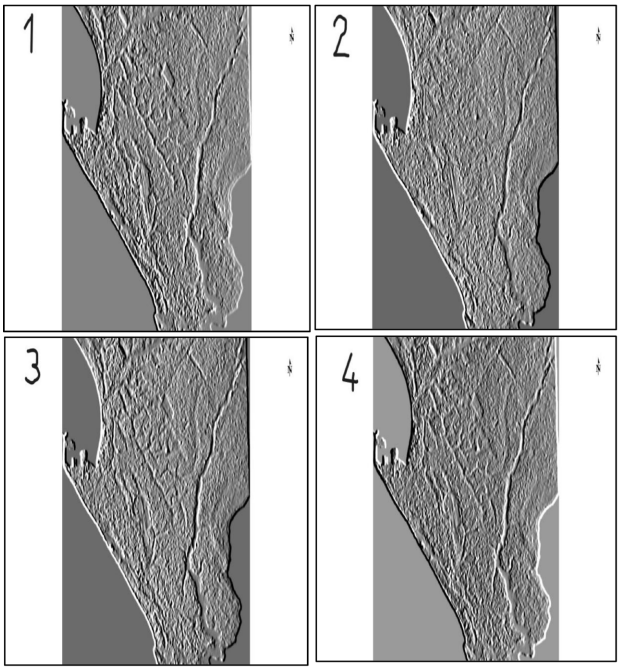

Figure 9. Results obtained by applying Convolution to the images above (Sobel filter: 1. PCA_{234}; 2. PCA_{567}; 3. PCA_{6710} and 4. PCA_{671011}) in a NW-SE direction and at an angle 135˚.

f) Result of Yesou's filter by applying the Convolution of morphology

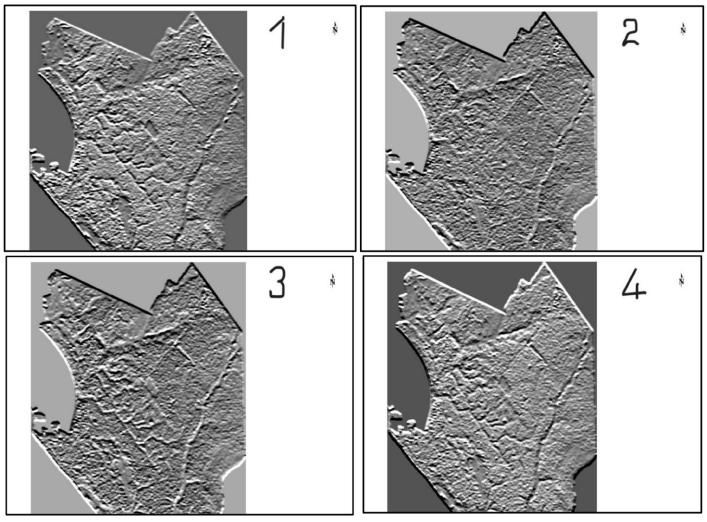

Figure 10. Results of the Yesou filter en applying Convolution to the images above: 1. PCA_{234}; 2. PCA_{567}; 3. PCA_{6710} and 4. PCA_{671011}.

4.1.3. Results of the Lineaments Maps

Figure 11 below shows the map of lineaments extracted manually on QGIS. There are 210 lineaments mapped, the longest measuring 11.63 km (maximum) and the

shortest 0.77 km (minimum).

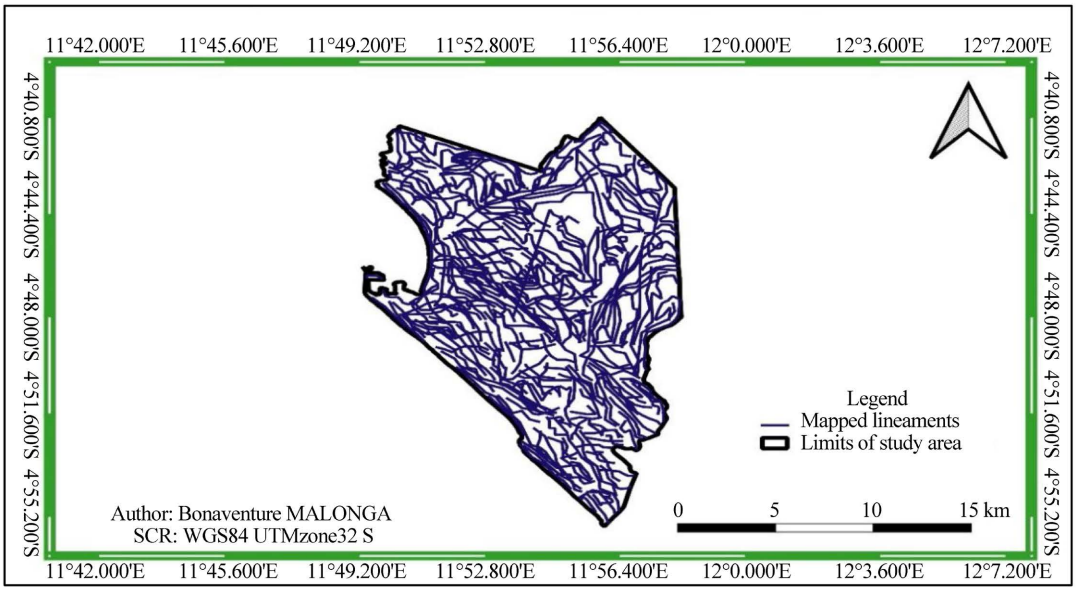

Figure 11. Result of the manual extraction of the lineaments map using the Raster module in QGIS.

4.1.4. Results Statistical Data Selection for the Development of the Final Lineament Map: Verification and Validation

The figures below show the distribution frequencies of the lengths of the lineaments, resulting from each digital processing, on the Pareto diagram.

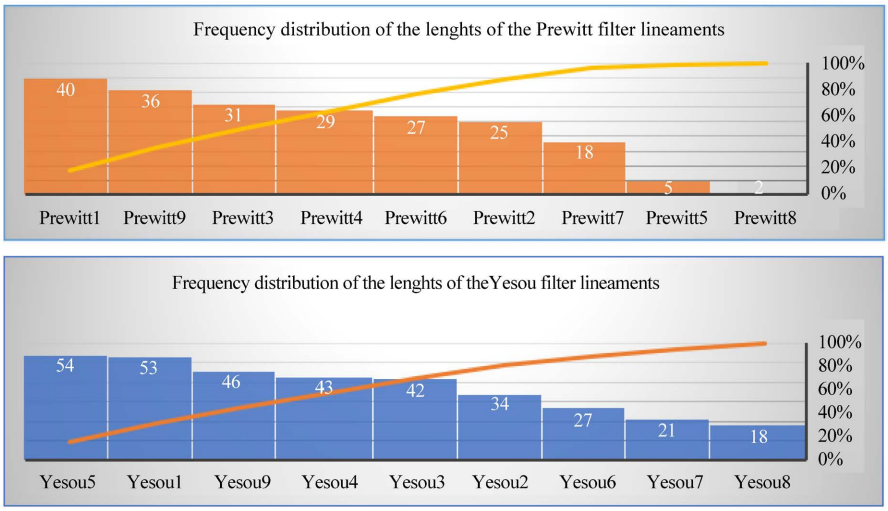

Figure 12. Results of Pareto diagrams of Prewitt filter and Yesou filter.

Figure 12 shows the Pareto diagram for data from the Prewitt and Yesou filters. Analysis of this figure allowed us to retain the lineaments of the first principal components of ACPs 2, 3, and 4 of ACP234 from the Prewitt filter and band 4 of the raw scene.

Analysis of Figure 13, obtained using the Sobel filter in the E-W and NW-SE

directions, enabled the first components of the PCA of bands 2, 3 and 4 and the ratio of bands 5 and 7 to be retained.

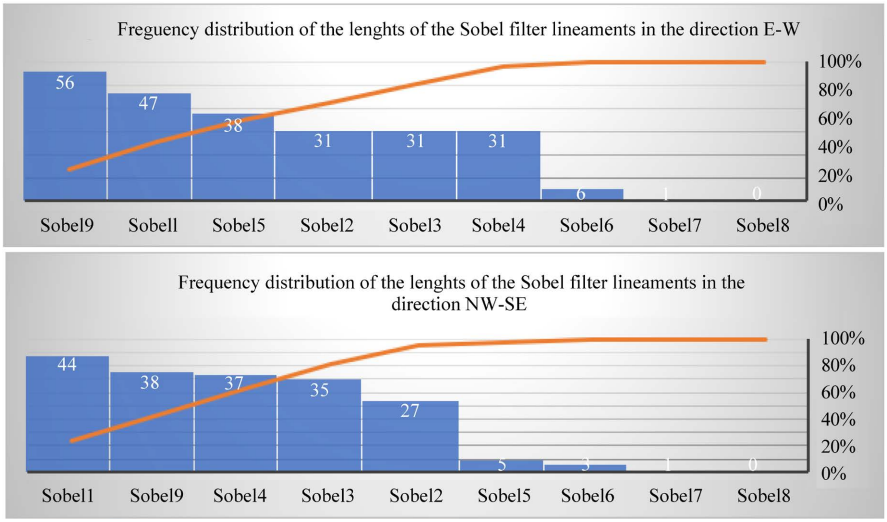

Figure 13. Results of Pareto diagrams of E-W and NW-SE lineaments.

4.1.5. Results of Automatic Lineament Merge Maps, Total Merge (Manual and Automatic) and Total Merge after Tectonic Synthesis

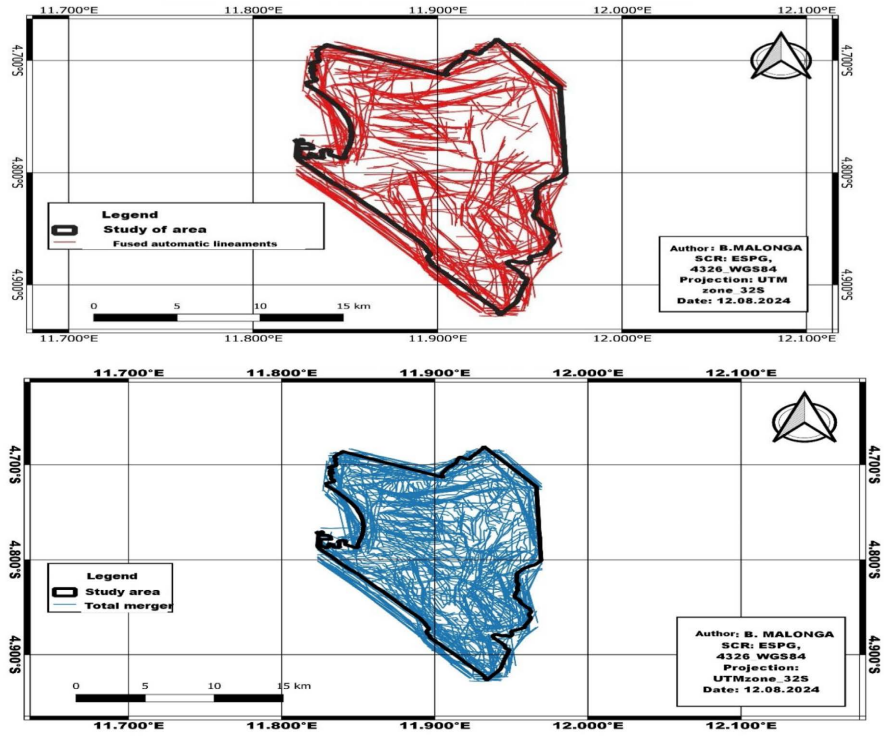

Figure 14. Results of 1. total merging of lineaments (automatic) and 2. total merging (automatic and manual).

Figure 14 shows the fusion maps of the automatic lineaments and the total fusion

map of the lineaments (automatic and manual). The automatic lineament fusion map (1) is the result of combining 21 maps, which enabled 859 lineaments to be extracted. However, the total fusion map of automatic and manual lineaments (2) enabled 1120 lineaments to be mapped.

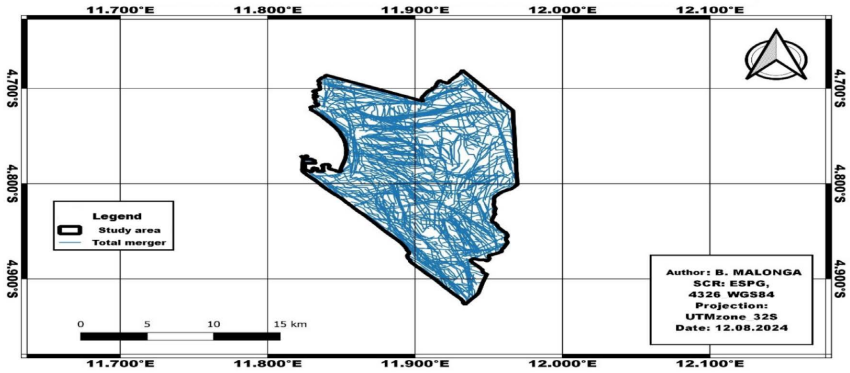

Figure 15. Result of the total fusion map after tectonic synthesis.

Figure 15 shows the total fusion map of the lineaments after tectonic synthesis. The number of lineaments mapped after calculating their orientation and adapting them to the geological context, where a total of 366 lineaments were removed, is 754.

4.1.6. Result of Superimposing the Total Fusion Map of Lineaments after Synthesis onto the Topographic Map from Google Earth Pro

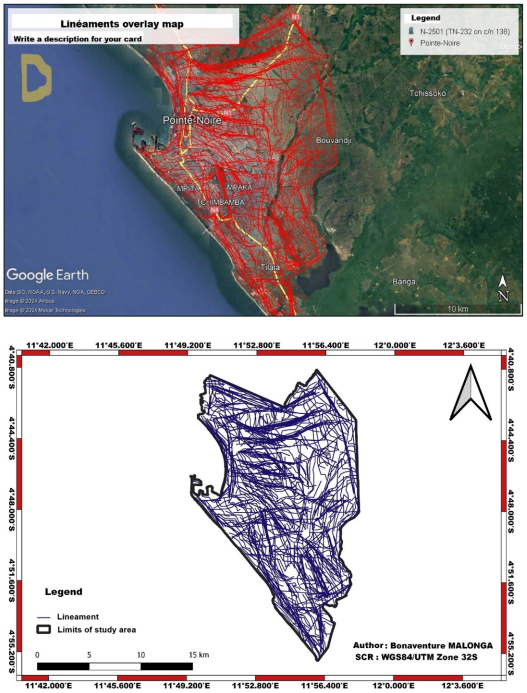

Figure 16. Result of 1. the lineaments assumption map mapped onto the high-resolution topographic map from Google Earth Pro and 2. the final lineament map of the study area.

Figure 16 shows the map obtained by superimposing mapped lineaments onto the high-resolution topographic map (1) and the final lineament map of the study area (2). Superimposing the summary lineament map onto the high-resolution topographic map (maximum quality: 8192x4930, Data SIO, NOAA, US Navy, NGA, GEBCO, 2024 Airbus image, Maar Technologies) on Google Earth Pro enabled us to validate the latter, after removing lineaments deemed non-geological. The final lineament map of our area thus contains 750 lineaments.

Table 4 shows the Comparaison of the LINE algoritm parameters with those of previous works.

Table 4. Comparaison of the LINE algoritm parameters with those of previous works.

Works	RADI (pixel)	GTHR (pixel)	LTHR (pixel)	FTHR (pixel)	ATHR (angle)	DTHR (pixel)
Default values	10	100	30	03	30	20
Kocal and al., 2004	12	25 - 60	20 - 30	03	20	01
Abdullah and al., 2013	10	100	30	03	30	20
G.C. Adon and al., 2014	20	90	50	10	15	100
G.C. Adon and al., 2019	20	90	50	10	15	100
A.K. Kouamé and al., 2023	24	40	50	05	20	120
B. Malonga, 2024	50	100	50	50	30	100

4.1.7. Correlation Results, Lineament Concordance

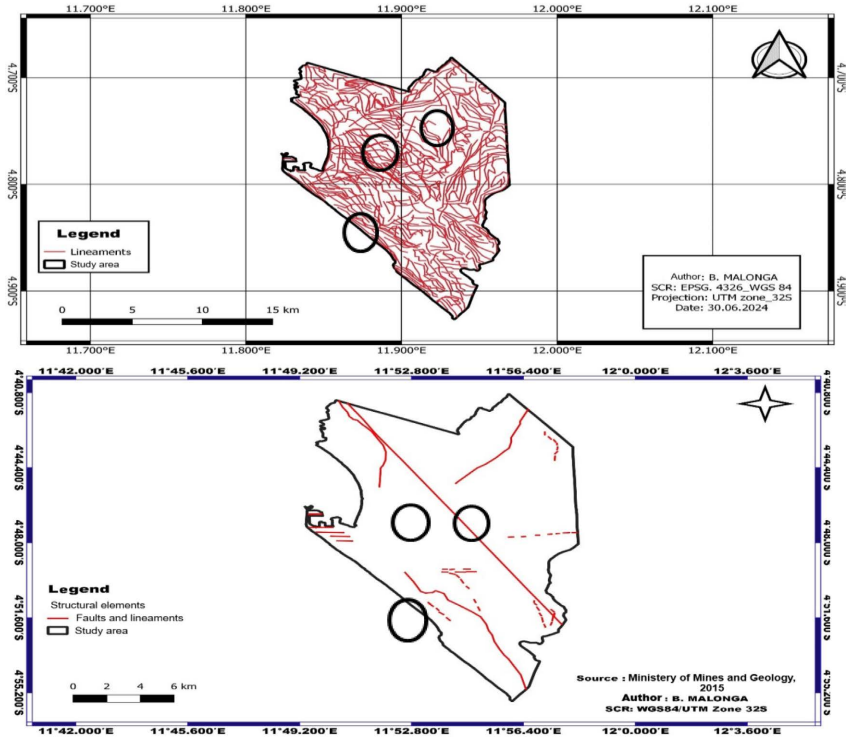

Figure 17. Result of 1. the correlation of linear structures between the SRTM image of the study area and 2. the gological map of Pointe-Noire, 2015.

Figure 17 shows the correlation map of linear structures between the SRTM image of the study area (1) and the 2015 geological map of Pointe-Noire (2).

4.1.8. Results of Density Maps of Mapped Lineaments and Lineaments Extracted from the Geological Map of Pointe-Noire

Figure 18 shows the correlation between the mapped lineaments and the lineaments extracted from the 2015 geological map of Pointe-Noire.

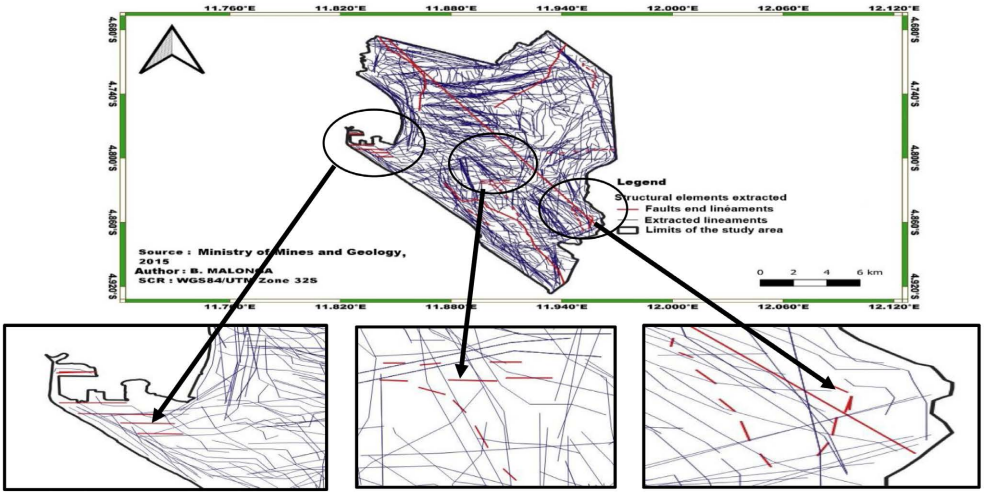

Figure 18. Result of the concordance between the mapped lineaments and the lineaments extracted from the 2015 Pointe-Noire geological map.

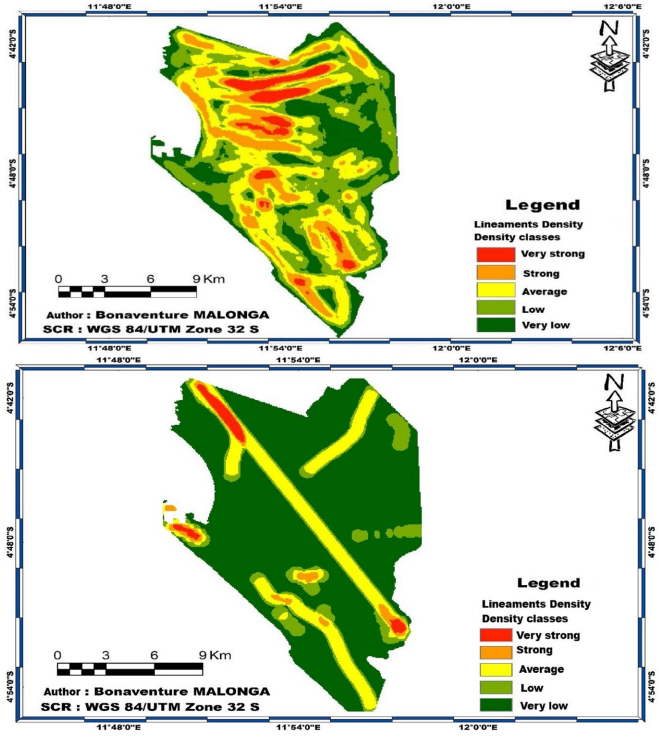

Figure 19. Results of 1. the comparison of the densities of the mapping lineaments in the study area and 2. the lineaments extrated from the 2015 Pointe-Noire geological map.

Figure 19 shows a comparison of the densities of the mapped lineaments (1) and the lineaments extracted from the 2015 geological map of Pointe-Noire (2).

4.2. Interpretation and Discussion of Results

Lineaments are geological features of various shapes whose influence has been felt for millions of years during successive tectonic phases. They represent geological objects or alignments of geological objects that are sufficiently close to the topographical continuities or geomorphological structures inherited from ancient topographies [31].

The results of radiometric and atmospheric corrections reveal an improvement in radiometric quality, which provides a very accurate analysis of the data and shows a significant reduction in atmospheric effects, making the image clearer and more uniform (Figure 4).

Textural analysis applied to PCA_{234} and band 4 (Figure 5), this band is selected for its reliability in structural analysis and lithological discrimination [3] [11] due to its sensitivity to the slightest variations in grey tones in the image generated (homogeneity, dissimilarity and average) to highlight the main structural elements, the results of which are presented in (RGB).

The results obtained with colour compositions, directional filters on selective PCA, band ratios and raw scenes enabled us to automatically and manually extract the lineaments from our study area. The study area has fractures or lineaments. Selective PCA shows the differences in the main characteristics of the scenes, facilitating the interpretation of spatial data and allowing the visualisation of certain lineaments in the study area, due to the presence of fractures (Figure 6). Some fractures have already been detected, most of which correspond to the surface hydrographic network. It can also be seen that PCA_{671011} is better at reading the pixels of the clouds contained in the image (Figure 6). Textural analysis of PCA_{234} and B4 reveals important information about surface structures, and the results of this analysis, presented in the form of a colour composition, prove to be valuable data for the automatic extraction of lineaments. Indeed, the linear structures observed in the PCA_{234}. Textural analysis reveals the heterogeneity of the geological formations in the study area. This heterogeneity reveals that the Sialivakou clays, the Pointe-Noire marls and the Pointe Indienne marls have more fractures (hydrocarbon refuge zones). The results obtained from the various stages of satellite image processing show an enhancement of the linear structures in the study area, which are then mapped, enabling us to respond to and highlight our project. The water tables contained in the subsoil are fed by surface waters. However, for these to be fully fed, there must be structures on the surface that promote this connection or correlation. Thus, surface fracture zones correspond to preferential zones through which surface water will feed underground water tables or aquifers by infiltration followed by percolation. The works of [16] [17] [19] have shown the existence of a correlation between fractures and hydrography, suggesting that the lineaments extracted from a satellite image are closely related to underground re-

sources. Given that we are working on Landsat 8 OLI images, we can confirm the works of [8] [19] [32] [33]. The lineaments mapped in our area over several orders of magnitude and vary in length and size, in accordance with the works of [4] [9] [13] [17]. PCA selectives make it possible to reduce the dimensionality of spectral data while retaining the most significant variability. The four PCA (PCA_{234}; PCA_{567}; PCA_{6710} et PC_{671011}) were used to capture the spectral variability of the images. This selection aims to maximise the relevant information for the analysis of lineaments and other geological structures. The results reveal that the principal components make it possible to differentiate geological structures from spectral anomalies.

However, it should be noted that only the PCA_{234} et PCA_{671011} reveal significant distinctions in textures and lineaments, as presented in **Figure 6**, in accordance with the work of [11] [15]; [8] [20] show that the application of textual analysis to PCA_{234} and to individual bands 4 and 7 reveals notable variations in fracture distribution, which is fundamental to the identification of lineaments. Analysis of the results obtained by our band ratios shows that they improve the contrast of different surface characteristics, thereby facilitating the identification of lineaments (**Figure 7** to **Figure 8**). Indeed, ratio calculations are sensitive in the vegetation cover. The use of these multiple band ratios provides a comprehensive and detailed view of the surface area of our study platform. Several Sobel filters were presented according to a preferred direction in line with the tectonic context of the study area and Yesou (**Figure 9** and **Figure 10**) were used for extraction automatic.

Analysis of the directional filters on PCA, band ratios, colour compositions and raw scenes shows not only the orientations N-S of the lineaments but also the longest ones, the longest or highest lineaments is 21.63 km revealing the orientation E-W of the Sobel filter and filter directional (**Table 2**), and values used of the parameters of LINE module (**Table 3**), whose fusion map has 1120 lineaments (the 210 lineaments from the lineament map extracted manually with SRTM tiles, see (**Figure 11**) according to the statistical data table (**Figure 12** and **Figure 13**), the Sobel filter has more lineaments than gradient filters wit 859 lineaments, where as the Yesou filter 338 lineaments. Of the 1120 lineaments 62 were removed following adaptation to the tectonic context of the study area, we also removed 304 lineaments located at the edges of the lineament map, leaving 754 on the lineament map after tectonic synthesis, 4 lineaments were then removed on Google Earth Pro, leaving only 750 (**Figure 14** to **Figure 15**) to finally obtain the final lineament map by superimposing it on the high-resolution topographic map (8192x4930, Data SIO), (**Figure 16**). **Table 4,** which is a comparative study with the parameters from previous studies reveals the different figures for the parameters chosen based on the results we obtained automatically (**Table 4**). The Pareto statistical in EXCEL enabled the selection of reliable data from the automatically extracted lineaments. Superimposing this data on the satellite data the study area makes it possible to identify a number of lineaments corresponding to the mapped faults (**Figure 17** and **Figure 18**). These lineaments derived from satellite images

are perfectly superimposed or slightly offset in relation to structural elements on the ground, as described in the works of [20]. In the same vein, we compared the densities of lineaments between the structural elements of the Pointe-Noire geological map [24]. The density maps show five (5) classes (very low, low, medium, high and very high) and reveal the predominance of directions N-W and NW-SE (**Figure 19**). The 2015 geological map of the Pointe-Noire sheet presents cartographic data used since 1980, with imagery from 2020. There has been an increase in the number of lineaments over the past 5 years (2015 to 2020) or 40 years (1980 to 2020) due to the acquisition of high-resolution satellite data and various advanced digital techniques. We note that the large number of features identified is the result of adapting to the removal of other lineaments that do not conform to the context.

5. Conclusion

This work has enabled us to assess the contribution of remote sensing to groundwater prospecting: case of the city of Pointe-Noire. The various techniques for processing satellite images (Landsat 8 OLI and SRTM) were applied to our study area (selective PCA, textural analysis, band ratio, normalised indices, colour compositions, directional filters and gradient filters). Principal component analysis reduced the spectral images to four selective PCA containing the maximum amount of information from the analysed data set and correlated the different bands that showed a good correlation. The band ratios and normalised indices reveal the different contrasts that made it possible to distinguish the linear structures of our study platform. Directional filtering and gradient filters enhance linear structures. The complete merging of data from automatic extraction with manual extraction (shading applied to SRTM images) resulted in improved mapping of the study area. Remote sensing undoubtedly contributes to the mapping of geological hazards in our study area, and the map produced can serve as a basis for hydrogeological and hydraulic programmes. The data from the density map (final lineament map) must be taken into *i.e.* the dominant NW-SE and E-W orientations to the context of the study area, where the well data can be plotted by the future location of the wells in order to establish a correlation with the aim of obtaining either a hydrogeological or the wells and the mapped lineaments.

Conflicts of Interest

The authors declare no conflicts of interest regarding the publication of this paper.

References

[1] IGIP GmbH (2008) Report on Drinking Water Supply in the City of Pointe-Noire. https://www.gitec-consult.com/

[2] Biémi, J. (1992) Contribution to the Geological and Hydrogeological Study, Using Remote Sensing, of the Sub-Sahelian Watersheds of the Precambrian Basement of West African: Hydrostructural, Hydrodynamic, and Isotopic Characteristics of the

Discontinuous Aquifers of the Granitic Rift Valleys of the Upper Marahoué (Côte d'Ivoire). Doctoral Thesis in Natural Sciences, University of Abidjan.

[3] Kouamé, K.F., Gioan, P., Biémi, J. and Affian, K. (1999) Method for Mapping Discontinuities in Images: Example of the Semi-Mountainous Region in Western Côte d'Ivoire. *Remote Sensing*, **1**, 139-156.

[4] Lasm, T. (2000) Hydrogeology of Fractured Reservoirs in the Bedrock: Statistical and Geostatistical Analysis of Fracturing and Hydraulic Properties. Application to the Mountainous Region of Côte d'Ivoire Archean Domain. Doctoral Thesis, University of Poitiers, 272 p.

[5] Llyod, J.W. (1999) Water Resources of Hard Rock Aquifers in Arid and Semi-Arid Zones. UNESCO.

[6] Jackson, T.J. (2002) Remote Sensing of Soil Moisture: Implications for Groundwater Recharge. *Hydrogeology Journal*, **10**, 40-51. https://doi.org/10.1007/s10040-001-0168-2

[7] Kresic, N. (1994) Remote Sensing of Tectonic Fabric Controlling Groundwater Flow in Dinaric Carst. *Proceedings of the* 10*th Thematic Conference on Geologic Remote Sensing*, San Antonio, 9-12 May 1994, 161-167.

[8] Miyouna, T., Bazebizonza Tchiguina, N.C., Essouli, O.F., Kempena, A., Nkodia, H.M.D. and Boudzoumou, F. (2020) Mapping of the Inkisi Group Lineaments in the Republic of Congo Using Satellite Image: Hydrogeological and Mining Implications. *Afrique Science*, **16**, 68-84.

[9] Youan, T.M., Lasm, T., Jourda, J.P., Mouame, K.F. and Razack, M. (2008) Mapping Geo-Logical Hazards Using Landsat-7 ETM+ Spectral Imagery and Analysis of Fracture Network in the Precambrian of the Bondoukou Region (Northeast Côte d'Ivoire). *Remote Sensing Journal*, **8**, 119-135.

[10] Sorokoby, M.V., Saley, M.B., Kouamé, F.K., Djagoua, E.V., Bernier, M., Affian, K. and Biémi, J. (2010) Use of Landsat ETM+ and SIRS Images for Linear and Thematic Mapping of Soubre-Meagui. *Remote Sensing Journal*, **9**, 209-223.

[11] Hammad, N. (2016) Geological Mapping and Lineament Analysis of the El Kseïbat Region (South-Western Sahara) Based on Satellite Imagery: Implication for Mineral Exploration. Doctorale Thesis, University Kasdi Merbah-Ouargla, 87-132.

[12] Soro, D.D. (2017) Characterisation and Hydrogeological Modelling of an Aquifer in a Bedrock Environment: The Case of the Sanon Experimental Site (Central Plateau Region of Burkina Faso). Joint Doctoral Thesis, Pierre and Marie Curie University, Paris 6 (France) and International Engineering (2iE), 303 p.

[13] Moukolo, N. (1992) Current State of Knowledge on the Hydrogeology of Congo Brazzaville. *Hydrogeology*, No. 1-2, 47-58.

[14] Bodin, J. and Razack, M. (1999) Image Analysis Applied to the Automatic Processing of Fracture Fields. Geometric Properties and Scaling Laws. *Bulletin de la Société Géologique de France*, **170**, 579-593.

[15] Youan, T.M., De Lasme, O., Baka, D., Lasm, T., Jourda, J.P. and Biémi, J. (2015) Analysis of the Hydrodynamic Properties of the Fractured Aquifer of the Paleoproterozoic Basement: Assistance in Supplying Drinking Region (Northeast Côte d'Ivoire). *International Journal of Innovation and Applied Studies*, **13**, 561-580.

[16] De Dreuzy, J.R. (2000) Analysis of the Hydraulic Properties of Fracture Networks. Discussion of Flow Models Compatible with the Main Geometric Properties. Doctoral Thesis, University of Rennes 1, 217 p.

[17] Lasm, T. and Razack, M. (2001) Scale Laws in the Weathering of Hard Crystalline

Rocks and in the Associated Hydrographic Network. *Proceedings of the Paris Academy of Sciences*, *Earth and Planetary Sciences*, **333**, 225-232.

[18] Kouamé, K.F., Penven, M.J., Kouadio, B.H., Saley, M.B. and Gronayes, C.C. (2006) Contribution of Terra Aster Images and a Digital Elevation Model to the Morpho-structural Mapping of the Toura Massif (Western Côte d'Ivoire). *Remote Sensing*, **6**, 103-121.

[19] Yao, T.K. (2009) Hydrodynamics in the Crystalline and Crystallophyllian Bedrock Aquifers of Southwestern Côte d'Ivoire: The Case of the Soubré Department. Contributions from Remote Sensing, Geomorphology and Hydrogeochemistry. Doctoral Thesis, University of Cocody.

[20] Ezzine, I., Zargouni, F. and Ghanmi, M. (2012) Linear Analysis of Landsat-TM and SPOT Images of the Central-Northern Atlas: Mapping the Extension SW of the Scar Left by Zaghouan. *Remote Sensing Journal*, **10**, 199-211.

[21] Jofack Sokeng, V.C., Kouamé, K.F., Youan, T.M. and Saley, M.B. (2014) Extraction of Lineaments from Satellite Images Using Neural Network: Contribution to the Structural Mapping of the Precambrian Bedrock in the Bondoukou Region (North-East Côte d'Ivoire). *Revue Scientifique Internationale de la Géomatique*, **1**, 4-17.

[22] Vennetier, P. (1968) Pointe-Noire and the Coastline of the Republic of Congo. https://horizon.documentation.ird.fr/exl-doc/pleins_textes/divers07-10/00829.pdf

[23] Samba-Kimbata, M.J. (1978) Climate of Lower Congo. Doctoral Thesis, Postgraduate Studies, University of Bourgogne, 280-281.

[24] Callec, Y., Lasseur, E., Le Bayon, B., Tchieblemont, Fullgraf, T., Gouin, J., *et al.* (2015) Explanatory Note for the Pointe-Noire Sheet at 1/200000. National Geological Mapping Programme. ORSTOM-TOTAL E&P Congo.

[25] Landsat (2020). https://landsat.usgs.gov/

[26] USGS (2020). https://earthexplorer.usgs.gov/

[27] Earth Observation Research Center/Japan Aerospace Exploration Agency (JAXA/EORC) (2021) ALOS Global Digital Surface Model (DSM) ALOS World 3D-30m (AW3D30) Version 3.2/3.1. Product Description Edition 1.2. https://www.eorc.jaxa.jp/ALOS/en/aw3d30/aw3d30v3.2_product_e_e1.2.pdf

[28] ALOS (2021). https://www.eorc.jaxa.jp/ALOS/en/aw3d30/data/index.htm

[29] Envi (2004) User's Guide. Research Systems Inc., ENVI 5.30, 1053 p. https://www.nv5geospatialsoftware.com/

[30] Chambaud, E. (2012) Pareto Chart, Applying the Pareto Principle and Analyzing It + Examples and Model. Project Management Blog. https://blog-gestion-de-projet.com/

[31] Yao, T.K., Fouché-Grobla, O., Oga, M.S.Y. and Assoma, V.T. (2012) Extraction of Structural Linéaments from Satellite Images and Estimation of Biases Induced in Meta-Morphosed Precambrian Bedrock Environments. *Remote Sensing Journal*, **10**, 161-178.

[32] Akokponhoue, B.H. and Lasme, O.Z. (2023) Contribution of Landsat OLI Imagery and Field Indices to the Structural Cartography of the Aquifer System of Black Volta Catchment in Côte d'Ivoire. *International Journal of Innovation and Applied Studies*, **40**, 520-531.

[33] Kouame, A.K., Ta, M.Y., Lasme, O.Z.D., Baka, D., Njeugeut, C.A.M. and Kouame, F.K. (2019) Analysis of Fracture Networks of the Black Volta Catchment in Côte d'Ivoire. *Journal of Geography*, *Environment and Earth Science International*, **19**, 1-14. https://doi.org/10.9734/jgeesi/2019/v19i230082